Nonlinear rock physics model for estimation of 3D subsurface stress in anisotropic formations: Theory and laboratory verification

Romain Prioul*, Andrey Bakulin‡, and Victor Bakulin**

ABSTRACT

We develop a rock physics model based on nonlinear elasticity that describes the dependence of the effective stiffness tensor as a function of a 3D stress field in intrinsically anisotropic formations. This model predicts the seismic velocity of both P- and S-waves in any direction for an arbitrary 3D stress state. Therefore, the model overcomes the limitations of existing empirical velocity-stress models that link P-wave velocity in isotropic rocks to uniaxial or hydrostatic stress.

To validate this model, we analyze ultrasonic velocity measurements on stressed anisotropic samples of shale and sandstone. With only three nonlinear constants, we are able to predict the stress dependence of all five elastic medium parameters comprising the transversely isotropic stiffness tensor. We also show that the horizontal stress affects vertical S-wave velocity with the same order of magnitude as vertical stress does. We develop a weak-anisotropy approximation that directly links commonly measured anisotropic Thomsen parameters to the principal stresses. Each Thomsen parameter is simply a sum of corresponding background intrinsic anisotropy and stress-induced contribution. The stress-induced part is controlled by the difference between horizontal and vertical stresses and coefficients depending on nonlinear constants. Thus, isotropic rock stays isotropic under varying but hydrostatic load, whereas transversely isotropic rock retains the same values of dimensionless Thomsen parameters. Only unequal horizontal and vertical stresses alter anisotropy. Since Thomsen parameters conveniently describe seismic signatures, such as normal-moveout velocities and amplitude-variation-with-offset gradients, this approximation is suitable for designing new methods for the estimation of 3D subsurface stress from multicomponent seismic data.

INTRODUCTION

Estimates of the underground stress field are required for a variety of subsurface activities including drilling, oil and gas production, and mining. Such estimates are usually obtained with the help of surface reflection seismic data (Dutta, 2002). Each method relies on a particular rock physics model that links seismic velocity to effective stress. The majority of these methods uses empirical models (Eaton, 1975; Eberhart-Phillips et al., 1989; Bowers, 1995) that share two common assumptions: (1) the vertical P-wave velocity is mainly controlled by the vertical effective stress and is almost unaffected by horizontal stresses, and (2) surface seismic provides an estimate of the vertically propagating P-wave velocity.

The first assumption remains valid in most cases; however, we demonstrate this is untrue for S-waves. Simple extension of existing P-wave techniques to shear waves is not possible. The second assumption is often violated because vertical velocities are never measured directly from reflection seismic data. Instead, vertical velocities are estimated from the analysis of normal-moveout (NMO) velocities that are dependent both on anisotropy of the subsurface, and vertical and horizontal stresses. Since many of the subsurface rocks exhibit intrinsic anisotropy (Thomsen, 1986; Wang, 2002) and are subjected to nonhydrostatic stress fields, seismically measured velocity is a poor estimate of the desired vertical velocity.

To account for intrinsic anisotropy and the effects of nonhydrostatic 3D stress and to extend the technique to shear waves, we take a different approach. Instead of searching for the best empirical approximation for a specific velocity at a given direction, we select nonlinear elasticity theory (Thurston, 1974) to relate the whole stiffness tensor to the whole stress

tensor. Having full mapping between two tensors provides a unique opportunity to compute the exact seismic signatures of interest [like NMO velocity or amplitude-variation-with-offset (AVO) gradient]. Nonlinear elasticity is not new to rock physicists, having already been applied in various contexts such as underground mines (Bakulin and Protosenya, 1981; Bakulin and Bakulin, 1992, 1999; Bakulin et al., 2000b), laboratory experiments (Guz et al., 1977; Johnson and Rasolofosaon, 1996; Winkler and Liu, 1996; Winkler et al., 1998; Bakulin et al., 2000b), and boreholes (Sinha and Kostek, 1996; Winkler et al., 1998; Sinha et al., 2000). Nonetheless, these attempts assumed that the background rock is isotropic, and they only use velocity measurements along a single direction. These conditions are not applicable to seismic data where rays span the whole spectrum of directions from vertical up to 45–60° and propagate in a material that is already intrinsically anisotropic even in the absence of stress.

In the first section of this paper, we revise the nonlinear elasticity theory involving an anisotropic background medium. We focus on the case of intrinsic transverse isotropy with a vertical symmetry axis (VTI), common in sedimentary basins. In the second and the third sections, we compare the predictions of nonlinear elasticity with experimental lab data on VTI samples of shale and sandstone. We study the behavior of all five VTI elastic constants as functions of stress. We test the predictions of nonlinear elasticity for the behavior of all velocities in all directions rather than in a single principal direction.

In the fourth section, we provide insight into the dependency of typical seismic signatures on all three principal stresses. Since most seismic signatures are more conveniently described in terms of the Thomsen anisotropic coefficients rather than stiffness tensors (Thomsen, 1986; Tsvankin, 2001), we develop the weak-anisotropy approximation that expresses the Thomsen parameters as function of stress magnitudes and the nonlinear constants. Application of this approximation is demonstrated by comparing the predicted and laboratory-measured Thomsen parameters as a function of stress for a Jurassic shale and a Colton sandstone.

THEORY

The effective elastic stiffness tensor as a function of stress can be described by the equations of nonlinear elasticity (Thurston, 1974). Nonlinear elasticity is a continuous-medium theory derived from first principles. In contrast to conventional linear elasticity, where the potential energy is a quadratic (second-order) function of strains, nonlinear elasticity includes cubic (third-order) terms that account for the change in acoustic properties with stress. These terms give rise to the so-called "third-order (nonlinear) elastic constants." Likewise, conventional (linear) elastic coefficients are sometimes called "second-order elastic constants." Here, we assume simple nonlinearity when elastic coefficients are functions of the stress state and not the stress history; that is, we do not consider the effect of hysteresis in large stress changes.

When small-amplitude waves propagating in a prestressed medium are considered, three configurations may be distinguished: (1) a *reference* state describing the medium in some starting configuration that is often (but not necessarily) taken to be unstressed, (2) an *intermediate* state describing the deformed state of the medium after static stresses were applied

to a material in a reference configuration, and (3) a *current* state describing the material configuration during wave propagation in a statically stressed media. Stresses and strains induced by the transformation from the reference to intermediate states are usually much larger than the ones induced by wave propagation. Nonlinear elasticity theory keeps the higher-order terms in strain to describe this finite deformation, while wave perturbation is still linearized. Effective elastic properties under stress, $c_{ijk\ell}$, depend on the unstressed elastic constants, $c_{ij}^{(0)}$, the stress T_{ij} and strain E_{ij} tensors, and some nonlinear properties of the material or third-order elastic constants c_{ijk}. As our subject is wave propagation, we define these effective elastic constants "as coefficients in a linearized equation of motion, or, equivalently, as coefficients in formulas for the propagation velocities of small-amplitude waves" (Thurston, 1974, p. 226).

Full equations for the effective elastic constants of a stressed VTI solid in the reference configuration are given in Appendix A. After simplifications, equations (A-1) reduce to a description of an orthorhombic solid, according to the approximation

$$
\begin{aligned}
c_{11} &\simeq c_{11}^0 + c_{111}E_{11} + c_{112}(E_{22} + E_{33}), \\
c_{22} &\simeq c_{11}^0 + c_{111}E_{22} + c_{112}(E_{11} + E_{33}), \\
c_{33} &\simeq c_{33}^0 + c_{111}E_{33} + c_{112}(E_{11} + E_{22}), \\
c_{12} &\simeq c_{12}^0 + c_{112}(E_{11} + E_{22}) + c_{123}E_{33}, \\
c_{13} &\simeq c_{13}^0 + c_{112}(E_{11} + E_{33}) + c_{123}E_{22}, \quad (1) \\
c_{23} &\simeq c_{13}^0 + c_{112}(E_{22} + E_{33}) + c_{123}E_{11}, \\
c_{66} &\simeq c_{66}^0 + c_{144}E_{33} + c_{155}(E_{11} + E_{22}), \\
c_{55} &\simeq c_{44}^0 + c_{144}E_{22} + c_{155}(E_{11} + E_{33}), \\
c_{44} &\simeq c_{44}^0 + c_{144}E_{11} + c_{155}(E_{22} + E_{33}).
\end{aligned}
$$

Here c_{ij} are the effective elastic constants of a stressed media in the contracted Voigt notations. Five independent second-order elastic constants $c_{11}^0, c_{13}^0, c_{33}^0, c_{44}^0$, and c_{66}^0 describe the VTI background media in the absence of stress, with c_{12}^0 being the combination $c_{12}^0 = c_{11}^0 - 2c_{66}^0$.

One assumption made is that the direction of principal stress, T_{33}, is aligned with the vertical symmetry axis of the VTI medium, implying that, in these chosen coordinates, $T_{12} = T_{13} = T_{23} = E_{12} = E_{13} = E_{23} = 0$. A second assumption made is that the third-order tensor in equations (1) and (A-1) is implicitly isotropic, that is, is defined by the three independent nonlinear coefficients c_{111}, c_{112}, and c_{123} and the two combinations $c_{144} = (c_{112} - c_{123})/2$, $c_{155} = (c_{111} - c_{112})/4$ (Thurston, 1974). This latter assumption is discussed in Appendix B and further validated for the studied experimental samples.

JURASSIC NORTH SEA SHALE

Experimental measurements

As our first example, we take compressional and shear wave velocities measured on shale (Hornby, 1995, 1998) under control of both hydrostatic confining (P^c) and pore (P^p) pressure. The samples represent fluid-saturated shales of Jurassic age with bulk density $\rho = 2540$ kg/m³ and porosity $\phi = 11\%$. Unstressed shales generally exhibit transverse isotropy with

a vertical symmetry axis (x_3) orthogonal to the fine-bedding planes. This set of ultrasonic measurements (Hornby, 1998, Figure 8 and Table 4 for $P^p = 0$ MPa; Hornby, 1995, Figures 8.1 and 8.4, and Tables 8.1 and 8.2 for $P^p = 20$ MPa) includes velocities V_{ij} propagating along the x_i-axis with a polarization along the x_j-axis (V_{33}, V_{31}, V_{32}, V_{11}, V_{13}, V_{12}), and velocities propagating at 45° to the symmetry axis (V_{qP45}, V_{qSV45}, V_{qSH45}).

In a VTI media, velocities measured along the principal axes are related to the diagonal elements of the stiffness tensor by these simple equations:

$$c_{11} = c_{22} = \rho V_{11}^2 = \rho V_{22}^2, \tag{2}$$

$$c_{33} = \rho V_{33}^2, \tag{3}$$

$$c_{44} = c_{55} = \rho V_{23}^2 = \rho V_{32}^2 = \rho V_{13}^2 = \rho V_{31}^2, \tag{4}$$

$$c_{66} = \rho V_{12}^2 = \rho V_{21}^2. \tag{5}$$

The remaining off-diagonal term is then expressed as:

$$c_{13} = c_{31} = c_{23} = c_{32} = -c_{44}$$
$$+ \sqrt{\left(c_{11} + c_{44} - 2\rho V_{45}^2\right)\left(c_{33} + c_{44} - 2\rho V_{45}^2\right)}, \tag{6}$$

where V_{45} is the velocity measured at 45° relative to the axis of symmetry, either V_{qP} for P-wave or V_{qSV45} for S-wave.

The velocities measured conform (within experimental errors) to the VTI relationships. Therefore for $P^p = 20$ MPa, we have computed four out of five independent stiffnesses (Table 1) using equations (2)–(5). For $P^p = 0$ MPa, several additional measurements of velocities at 45° were also made. In this case, elements of the best-fit VTI tensor (Table 1) were obtained from an overdetermined system of equations by a least-squares inversion. The objective function was represented by the sum of the squared differences between the measured and predicted slownesses of all waves in all directions.

Estimation of the third-order elastic constants

For saturated rocks, we assumed that the velocities are controlled by the effective stress (T_{ij}), which we defined as the difference between the confining (P_{ij}^c) and the pore pressure (P^p),

$$T_{ij} = P_{ij}^c - \delta_{ij} P^p, \tag{7}$$

where δ_{ij} is the Kronecker delta function (we assume here that the Biot coefficient α, that should precede the pore pressure

Table 1. **Estimated second-order VTI elastic constants for a Jurassic North Sea shale under confining (P^c) and pore (P^p) pressures.**

P^c (MPa)	P^p (MPa)	c_{11}^0 (GPa)	c_{33}^0 (GPa)	c_{13}^0 (GPa)	c_{66}^0 (GPa)	c_{44}^0 (GPa)
5	0	33.9	22.8	15.0	9.7	5.1
10	0	36.5	24.6	15.7	10.8	5.9
20	0	39.9	27.4	16.6	12.1	7.0
40	0	44.0	30.1	17.4	13.5	7.9
60	0	45.8	32.1	18.2	14.2	8.5
80	0	46.7	33.4	18.7	14.5	9.0
35	20	39.2	27.1	—	11.8	6.6
70	20	44.3	31.5	—	13.7	8.2
90	20	45.7	33.0	—	14.2	8.8
110	20	46.7	34.3	—	14.5	9.2

term, is constant and equal to unity). Therefore, the stress term in all equations is understood everywhere as effective stress.

The data in Table 1 clearly exhibit distinctly different behavior at low and high effective stress, therefore, we divided the stress range into two intervals ($[T_1^c, T_2^c]_i$, $i = 1, 2$): 5–30 and 30–100 MPa. In the actual inversion, we used a slightly modified version of equations (A-1), (A-2), and (1). Instead of operating with unstressed stiffnesses $c^{(0)}$, it is more convenient to define some fixed new reference state conveniently located inside each stress interval more or less equivalent to a hydrostatic deformed or intermediate stress state. Then, the stiffnesses at this reference state, together with the third-order coefficients, describe the local behavior of the effective stiffness tensor in the vicinity of the reference state. This was achieved by a linear transformation of variables,

$$T_{ij} \to \Delta T_{ij}, \qquad E_{ij} \to \Delta E_{ij}, \tag{8}$$

where $\Delta T_{ij} = T_{ij} - T_{ij}^{(r)}$, $\Delta E_{ij} = E_{ij} - E_{ij}^{(r)}$ are the differences between stresses and strains in the current and reference states. Under such transformations, linear equations (A-1), (A-2), and (1) stay unchanged, provided that $c_{ij}^{(0)}$ in an unstressed state is replaced by $c_{ij}^{(r)}$ in a reference state. The third-order coefficients denote gradients in the stiffness-strain coordinates and they do not change their values under the linear transformation (8).

For the first stress interval, we chose a reference state at 10 MPa, whereas for the higher stress interval, we took 40 MPa. For each interval $[T_1^c, T_2^c]$, the four diagonal stiffness elements, computed by equations (2)–(5), were inverted for the three third-order constants $c_{111}, c_{112}, c_{123}$ by minimizing a least-squares misfit function,

$$\chi^2 = \sum_{T_1^c}^{T_2^c} \sum_{ij} \left[\frac{c_{ij}^{mes} - c_{ij}^{pred}}{\sigma_{ij}}\right]^2, \tag{9}$$

between measured c_{ij}^{mes} and predicted c_{ij}^{pred} stiffnesses. Even though we have only hydrostatic stress ($T_{11} = T_{22} = T_{33}$), we were able to estimate all three nonlinear constants due to VTI anisotropy of unstressed shale (see Appendix B for explanations). Since stiffnesses were considered as functions of only one pressure variable (effective stress), the measurements for both pore pressures 0 and 20 MPa were used simultaneously. The standard deviation (σ_{ij}) of the measured stiffnesses was taken as 2% of the measured value. The estimated third-order parameters are given in Table 2. Results show that the predictions fit the measured data well, i.e. within ±2% error (Figure 1). This proves that three "isotropic" third-order coefficients are sufficient to describe the four VTI stiffnesses in each stress interval.

As an independent check, we predict the remaining stiffness c_{13}, which was not used in the inversion of the nonlinear constants. We compare our prediction with the measured value c_{13}

Table 2. **Third-order elastic constants within a 99% confidence interval obtained from hydrostatic stress experiment on a North Sea shale.**

Hydrostatic (MPa)	$c_{111} \pm \Delta c_{111}$ (GPa)	$c_{112} \pm \Delta c_{112}$ (GPa)	$c_{123} \pm \Delta c_{123}$ (GPa)
5–30	-11300 ± 2900	-4800 ± 2500	5800 ± 4000
30–100	-3100 ± 600	-800 ± 500	40 ± 800

given in Table 1 (c_{13} estimation was possible because off-axes velocities V_{qP45} and V_{qSV45} were measured). Such a comparison is plotted in Figure 2 and confirms a good a posteriori prediction.

Error analysis.—Obtaining the best fit for the measured and predicted data demands that we retrieve the parameters of the model, some error estimates of those parameters, and a statistical measure of goodness of fit. The error on the estimated parameters can be obtained using confidence limits. We search for confidence levels and the shape of a confidence region, encompassing a stated percentage of probability. We used Monte-Carlo simulation with the χ^2 minimization method. First, the minimum value χ^2_{min} is found at parameters $\mathbf{a_0} = [c_{111}, c_{112}, c_{123}]$. Second, if the vector of parameters $\mathbf{a}$ is perturbed away from $\mathbf{a_0}$, then the region within which χ^2 increases by more than a set

amount $\Delta\chi^2 = \chi^2 - \chi^2_{min}$ defines some 3D confidence region around $\mathbf{a_0}$ (Press et al., 1986). In our case, this 3D region can be represented by ellipsoids. Figure 3 displays cross-sections of this ellipsoid for a low-stress range, and a similar picture can be drawn for high stress. We conclude that a global minimum exists. The 1D projections of the solid curves ($\Delta\chi^2 = 1, 4, 6.63$) on the corresponding axes contain 68.3%, 95.4%, and 99% of normally distributed data, respectively (Press et al., 1986). The error associated with the estimated third-order parameters in Table 2 are within a 99% confidence interval.

The error analysis shows that a small linear dependance exists between coefficient c_{111} and c_{123} (Figure 3), and that the confidence limits at high effective stress are approximately five times smaller than the ones derived at low effective stress (Table 2).

The large values of the error bars do not render the results meaningless. Being coefficients of higher-order terms, nonlinear constants should be many orders of magnitudes larger than the usual elastic moduli in order to have any effect on velocities. Spanning the whole range of a seemingly large range of uncertainty, we observe only 1–2% changes in the corresponding velocities. Therefore, the obtained uncertainty ranges are still meaningful in sense of predicting velocities with good seismic precision.

COLTON SANDSTONE

Experimental measurements

As our second example, we took ultrasonic measurements from Dillen et al. (1999) on a dry Colton sandstone placed in a triaxial stress machine. The Colton sandstone formation is an Eocene fluvial deposit located in north-central Utah, USA (bulk density $\rho = 2380$ kg/m^3, porosity $\phi = 13\%$).

At zero stress, the Colton sandstone also exhibits transverse isotropy with a vertical symmetry axis aligned with one of the directions of the triaxial machine (T_{33}). Equal compressive stresses were applied along the x_1- and x_2-axis directions to preserve the VTI anisotropy of the sample ($T_{11} = T_{22}$). The block
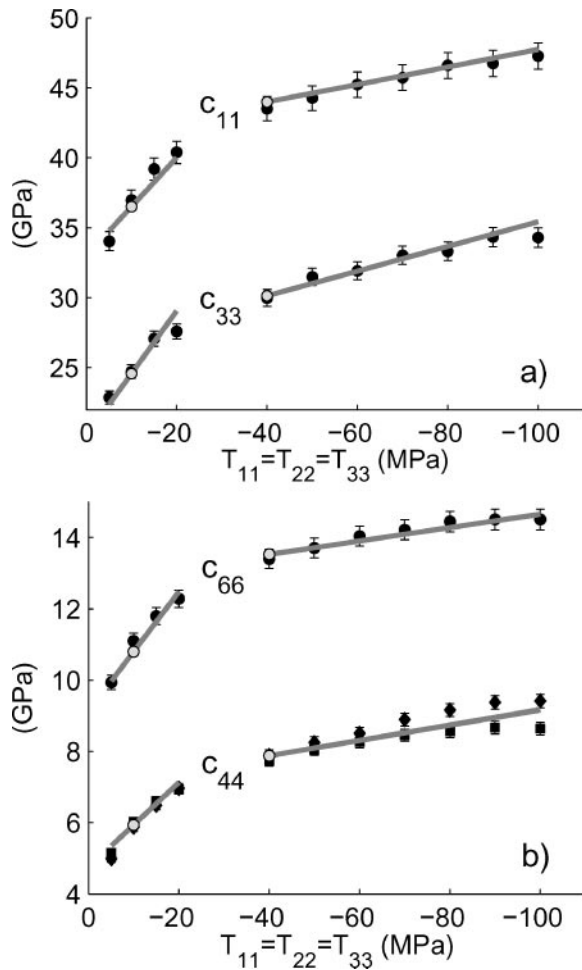

Figure 1. Effective elastic stiffnesses as a function of hydrostatic effective stress for the North Sea shale: (a) c_{11} and c_{33}, and (b) $c_{66} = \rho V_{12}^2$, $c_{44} = \rho V_{13}^2$ (■), and $c_{44} = \rho V_{31}^2$ (♦). The entire stress interval was divided into smaller intervals (5–30 and 30–100 MPa). Measured data are shown by points and predicted data [by equations (1)] are plotted as solid lines. For 5–30 MPa, the reference state (open circles) was taken at 10 MPa (Thomsen parameters $V_{P0} = 3.11$ km/s, $V_{S0} = 1.53$ km/s, $\epsilon = 0.24$, $\delta = 0.13$, $\gamma = 0.41$). For 30–100 MPa, it was taken at 40 MPa ($V_{P0} = 3.44$ km/s, $V_{S0} = 1.77$ km/s, $\epsilon = 0.23$, $\delta = 0.11$, $\gamma = 0.36$.)
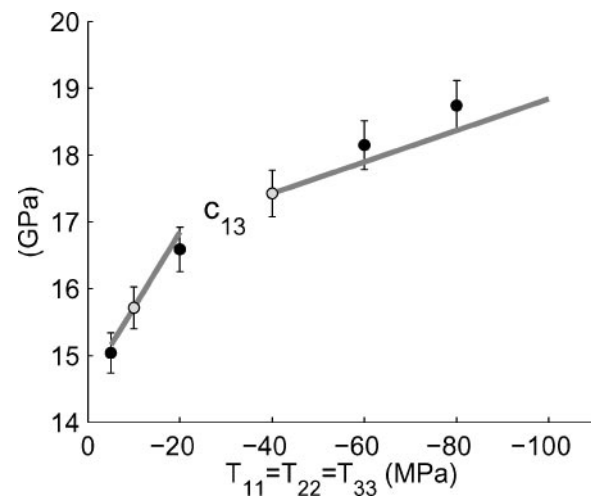

Figure 2. Measured (points) and predicted (lines) effective elastic stiffness c_{13} in two intervals of effective pressure (5–30 and 30–100 MPa) for North Sea shale. The prediction was done with equations (1), where parameters c_{111}, c_{112}, c_{123} were inverted from c_{11}, c_{33}, c_{44}, and c_{66}.

was subjected to an alternating load cycle as shown in Figure 4. The stress path contains both hydrostatic intervals (e.g., a–b, h–i) as well as nonhydrostatic (biaxial) ones (e.g., b–h). Therefore, we were able to compare the robustness in estimating the nonlinear coefficients at various types of stress states.

Input data from Dillen et al. (1999) consist of P- and S-wave velocities along the coordinate axes of the pressure cell (V_{11}, V_{22}, V_{33}, V_{12}, V_{21}, V_{13}, V_{31}, V_{23}, V_{32}) measured during the stress cycle (Figure 5).

Comparison of nonlinear constants at hydrostatic and biaxial loads

Because no velocity measurement was available at an oblique angle to the coordinate axes, we did not estimate the off-diagonal stiffness elements. The diagonal elements of the effective stiffness tensor under stress were estimated using equations (2)–(5). At each stress level, the measured veloc-

ities satisfied the approximate relationships (2)–(5), suggesting that the transverse isotropy was approximately preserved under biaxial loading.

The third-order elastic constants for the Colton sandstone were estimated following the same procedure used for the Jurassic shale. The reference state was selected at the start of the experiment, where $T_{11} = T_{22} = T_{33} = -0.7$ MPa for which the Thomsen parameters were estimated as $V_{P0} = 2.77$ km/s, $V_{S0} = 1.89$ km/s, $\epsilon = 0.05$, $\gamma = 0.03$. Thomsen parameter δ was not constrained by the measured velocities along axes and was taken as 0.05 in this study. Next, all stiffnesses at several stress levels are inverted for third-order coefficients using equations (A-1). To investigate how the stress state affects estimation of the third-order constants, we used velocities measured at different parts of the stress cycle. Results of the inversion (shown in Table 3) prove that nonlinear coefficients at hydrostatic (a–b, h–i), biaxial (b–c, d–e, f–g), and arbitrary (a–i) stress states are nearly identical. However, confidence
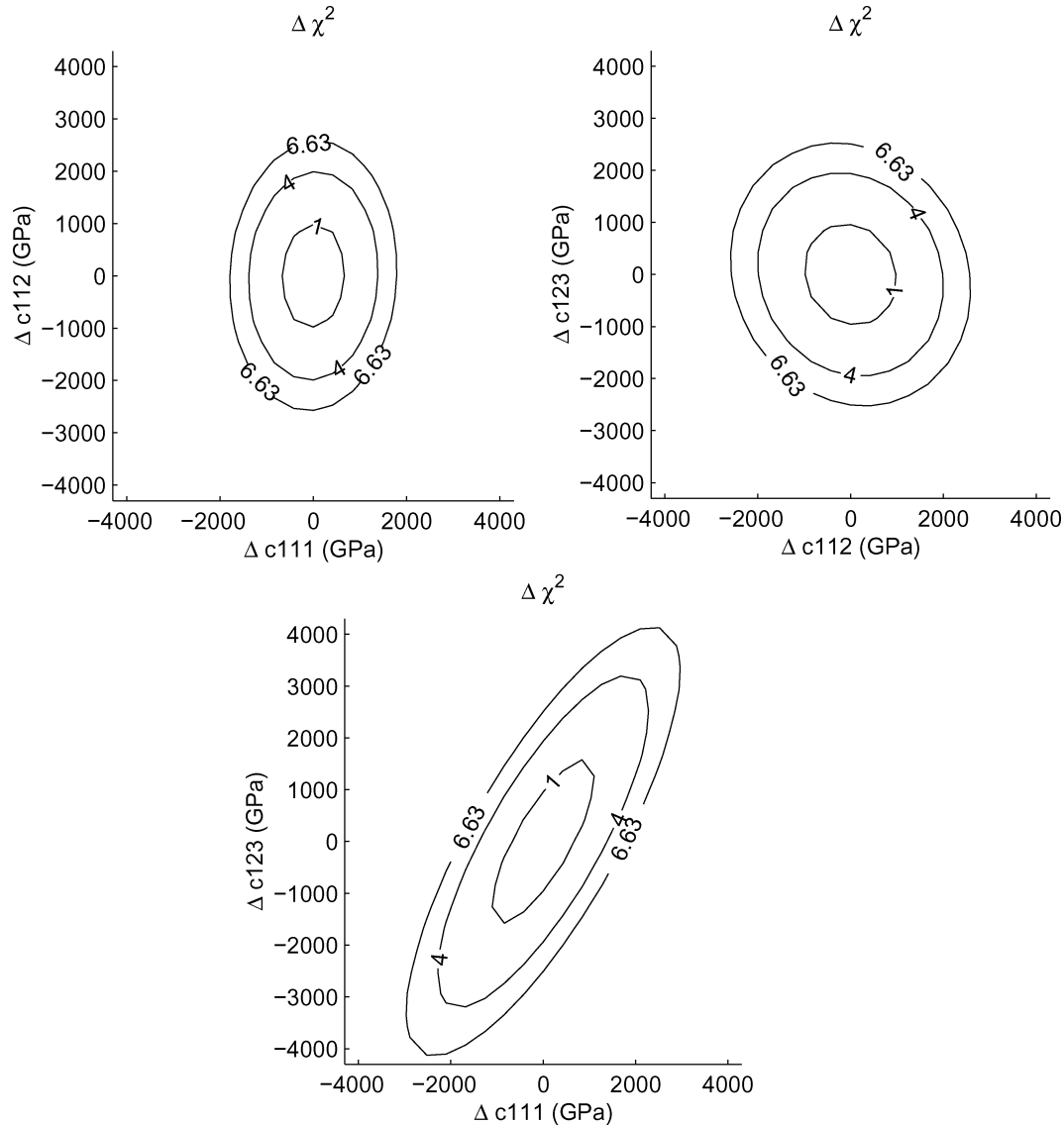

Figure 3. Cross-sections of the confidence ellipsoids by coordinate planes for the stress interval 5–30 MPa. Contours represent the variation of the misfit function $\Delta\chi^2 = \chi^2 - \chi^2_{min}$. The projection of the curves ($\Delta\chi^2 = 1, 4, 6.63$) on each 1D interval contain 68.3%, 95.4%, and 99% of normally distributed data, respectively.

limits in the arbitrary stress were approximately two to four times smaller (Table 3).

These results confirm the conclusion from Appendix B that even for relatively weak anisotropy (Thomsen parameters of the order of 0.05), hydrostatic stress experiments can be used to recover the correct values of all three nonlinear coefficients, albeit with larger uncertainty. Note that varying the unknown parameter δ for unstressed rock between 0 and 0.1 leads to almost the same values of third-order constants as in Table 3.

Comparison of measurements with predictions of the theory

To demonstrate the predictive power of the theory, we compare all measured stiffnesses for the entire stress cycle with the predictions of nonlinear elasticity computed using a single set of third-order coefficients obtained for path a–i (Table 3). Figures 6 and 7 demonstrate that three stress-sensitivity parameters capture the essential behavior of all measured stiffnesses within the acceptable level of errors (2% for stiffness or 1% for velocity).

Dependence of velocities on stresses acting in the propagation and polarization directions

On Figure 5 where T_{33} is constant and $T_{11} = T_{22}$ is increasing (paths d–e and f–g), we notice that, for P-waves, $V_{11} \sim V_{22}$ increase significantly while V_{33} has almost no variation. In con-

trast, shear velocities V_{31}, V_{32}, V_{13} and V_{23} have almost the same increase. Thus, P-waves are influenced predominantly by the stress in the propagation direction, whereas, S-wave velocity is almost equally influenced by the stresses both in the polarization and propagation directions. Since those directions are orthogonal, S-wave velocity may not be uniquely interpreted in terms of applied stress. This observation, confirmed also by Sarkar et al. (2003) on Berea sandstone, emphasizes the need for a model that properly honors the 3D nature of the Earth stress field. Figures 6 and 7 demonstrate that our model correctly describes the complex behavior of shear-wave velocity under realistic stress regime.

THOMSEN PARAMETERS OF STRESSED ROCKS

We showed that the behavior of the stiffness tensor under stress is well described by nonlinear elasticity in these two rock samples. However, the underlying equations are still too complex to prevent direct intuitive predictions on how each individual element of the stiffness tensor would behave under triaxial stress. Yet, we would like to be able to intuitively predict seismic signatures, such as NMO velocities and AVO gradients, largely controlled by the off-diagonal elements. We intend to permit such intuitive insight by utilizing a representation of the stiffness tensor using Thomsen (1986) parameters. Five elastic coefficients of VTI media are replaced by the vertical velocities V_{P0} and V_{S0} of P- and S-waves and the three dimensionless anisotropic parameters ϵ, δ, and γ (Thomsen, 1986):

$$V_{P0} \equiv \sqrt{\frac{c_{33}}{\rho}}, \quad (10)$$

$$V_{S0} \equiv \sqrt{\frac{c_{44}}{\rho}}, \quad (11)$$

$$\epsilon \equiv \frac{c_{11} - c_{33}}{2c_{33}}, \quad (12)$$

$$\delta \equiv \frac{(c_{13} + c_{44})^2 - (c_{33} - c_{44})^2}{2c_{33}(c_{33} - c_{44})}, \quad (13)$$

$$\gamma \equiv \frac{c_{66} - c_{44}}{2c_{44}}. \quad (14)$$

Table 3. Third-order elastic constants c_{111}, c_{112}, and c_{123} with 99% confidence interval for Colton sandstone estimated using different parts of stress cycle from Figure 4.

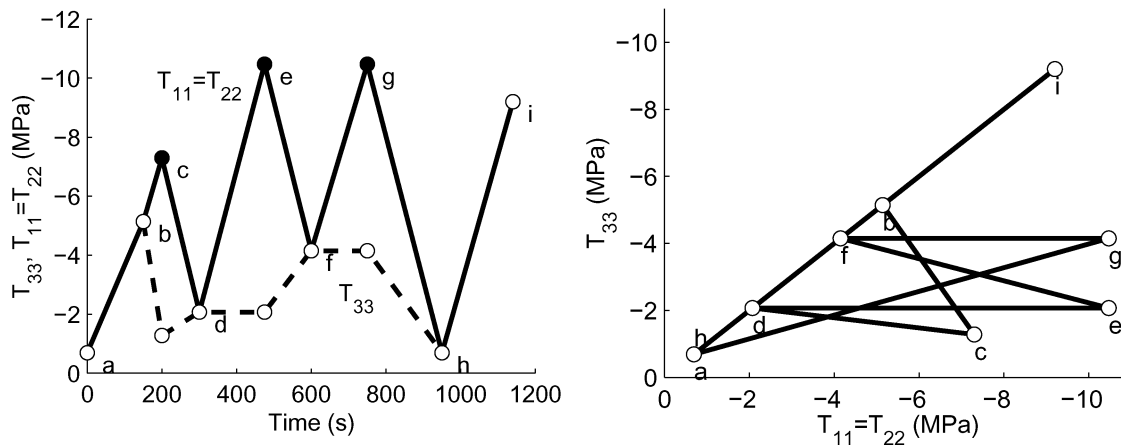| Stress (MPa)	$c_{111} \pm \Delta c_{111}$ (GPa)	$c_{112} \pm \Delta c_{112}$ (GPa)	$c_{123} \pm \Delta c_{123}$ (GPa)
Hydrostatic			
(a–b)	-7700 ± 3000	-1000 ± 2000	100 ± 4000
(h–i)	-7100 ± 2000	-1300 ± 1200	700 ± 2000
Biaxial			
(b–c)	-7600 ± 1500	-1400 ± 1000	500 ± 1500
(d–e)	-7400 ± 1200	-1400 ± 800	500 ± 1200
(f–g)	-7700 ± 1200	-1400 ± 800	700 ± 1500
Arbitrary			
(a–i)	-7400 ± 800	-1400 ± 500	600 ± 800

Figure 4. Biaxial stress cycle ($T_{11} = T_{22} \geq T_{33}$) applied to the block of Colton sandstone as a function of time (left) and stress path in the plane $[T_{11}, T_{33}]$ (right). Principal stresses T_{11} and T_{22} are maintained equal in order to preserve the transverse isotropy of the sample (data from Dillen et al., 1999).

The dimensionless parameters ϵ, δ, and γ represent the strength of the anisotropy. For isotropic media, they are equal to zero. The parameters ϵ and γ define the fractional difference between horizontal and vertical P- and S_H-wave velocities, respectively. The less intuitive parameter δ controls the NMO velocity of the P-wave for a horizontal reflector as well as the P-wave AVO gradient.

Exact expressions for the Thomsen parameters as a function of stress are more complicated than the formulas for the
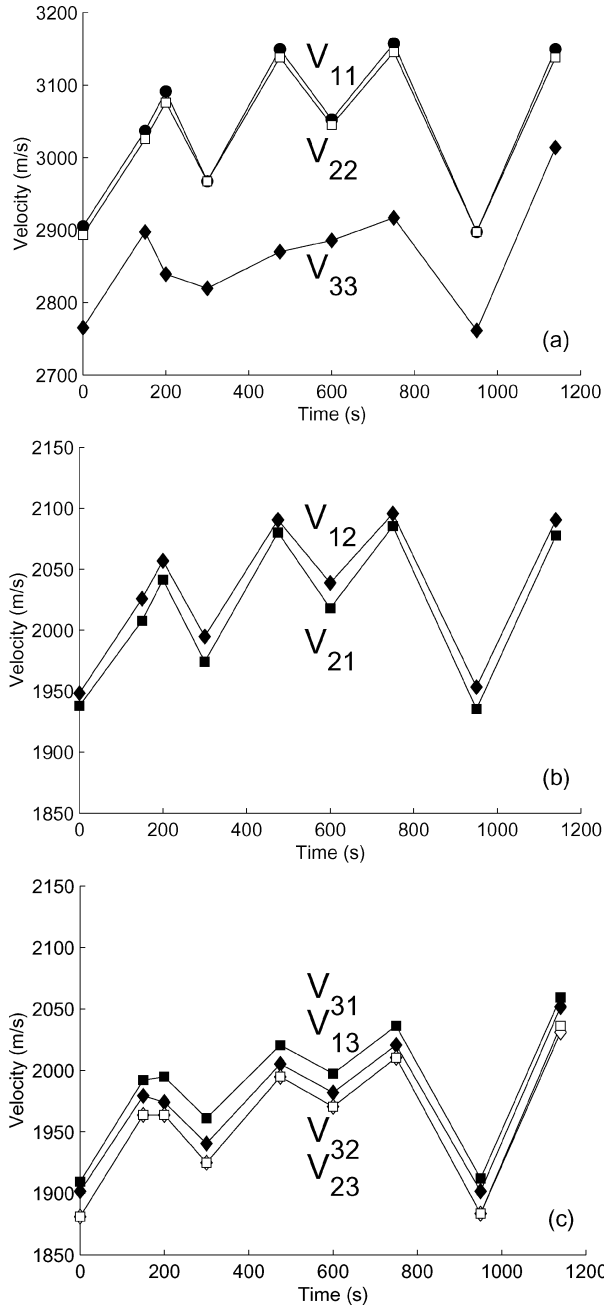

Figure 5. Measured compressional and shear wave velocities for Colton sandstone as a function of time during the load cycle (shown in Figure 4): (a) V_{11} (●), V_{22} (□), and V_{33} (♦); (b) V_{12} (♦) and V_{21} (■); (c) V_{23} (◇), V_{32} (□), V_{13} (♦), and V_{31} (■) (data from Dillen et al., 1999).
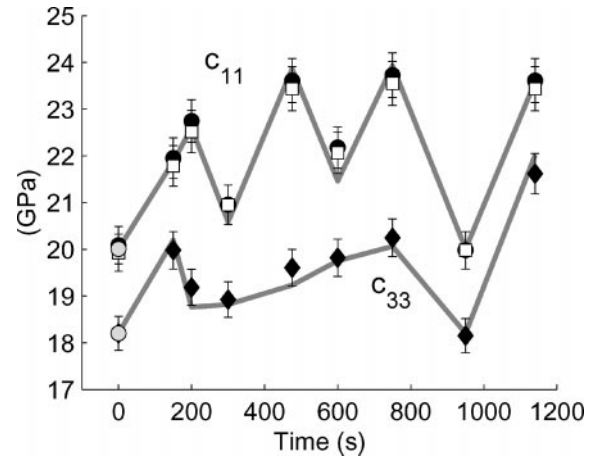

Figure 6. Measured (points) and predicted (lines) effective elastic stiffnesses $c_{11} = \rho V_{11}^2$ (●), $c_{11} = \rho V_{22}^2$ (□), and $c_{33} = \rho V_{33}^2$ (♦) for Colton sandstone. Error bars correspond to $\pm 2\%$ of measured stiffnesses. Only three parameters (c_{111}, c_{112}, and c_{123}) have been used to predict all stiffnesses under the entire loading cycle. The reference state (open circle) has been taken at zero time ($T_{11} = T_{22} = T_{33} = -0.7$ MPa).
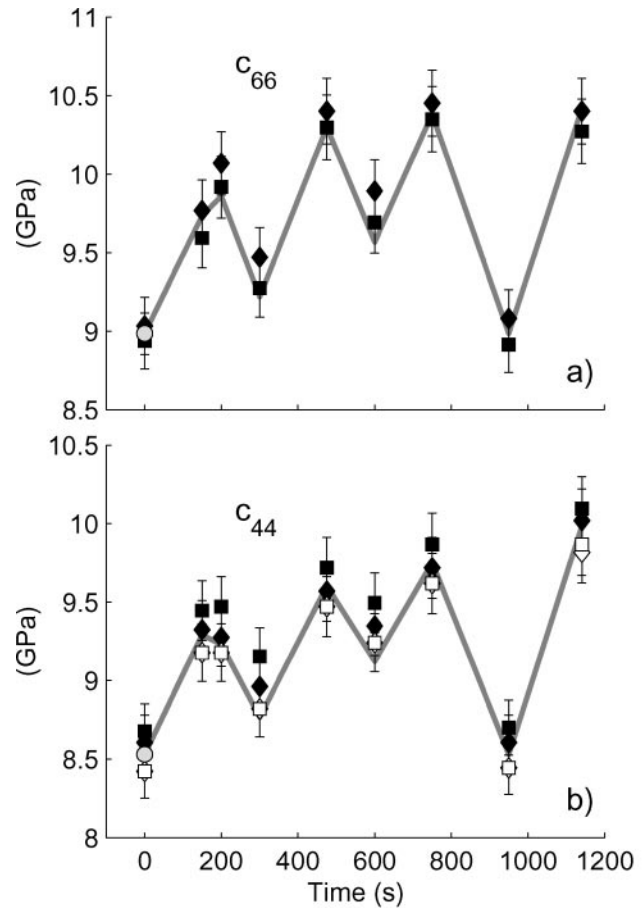

Figure 7. The same as Figure 6 but for stiffnesses: (a) $c_{66} = \rho V_{12}^2$ (♦) and $c_{66} = \rho V_{21}^2$ (■); (b) $c_{44} = \rho V_{23}^2$ (◇), $c_{44} = \rho V_{32}^2$ (□), $c_{44} = \rho V_{13}^2$ (♦), and $c_{44} = \rho V_{31}^2$ (■).

elements of the stiffness tensor from equations (A-1) and (1). However, the weak-anisotropy approximation of the Thomsen parameters allows one to obtain intuitive insight on the link between stress magnitudes and elastic properties, as well as stress magnitudes and seismic signatures.

Weak-anisotropy approximation

We limit our discussion only to experimentally observed effective VTI media due to a biaxial stress state ($T_{11} = T_{22} \neq T_{33}$) applied to an unstressed VTI rock. A more general analysis was performed for orthorhombic media caused by triaxial stress (Sarkar et al., 2003). Our method is similar to that applied to fractured media with anisotropic background (Bakulin et al., 2000a). We assume that each stiffness from equation (1) may be represented as

$$c_{ij} = c_{ij}^{(0)}(1 + \Delta_{ij}),\qquad(15)$$

where Δ_{ij} is the stress-induced contribution. In the weak anisotropy limit, we assume that all Δ_{ij}, along with the anisotropic parameters $\epsilon^{(0)}$, $\delta^{(0)}$, and $\gamma^{(0)}$ defined in the reference state, are small quantities of the same order. Linearizing the equations in these small quantities gives

$$\epsilon = \epsilon^{(0)} + \epsilon_{s-i}, \quad \epsilon_{s-i} = \frac{K_p}{2c_{44}^{(0)}}(T_{11} - T_{33}), \qquad(16)$$

$$\delta = \delta^{(0)} + \delta_{s-i}, \quad \delta_{s-i} = \frac{K_p}{2c_{44}^{(0)}}(T_{11} - T_{33}), \qquad(17)$$

$$\gamma = \gamma^{(0)} + \gamma_{s-i}, \quad \gamma_{s-i} = \frac{K_s}{2c_{44}^{(0)}}(T_{11} - T_{33}), \qquad(18)$$

where K_p and K_s are two quantities controlling the stress-induced part of P- and S-wave anisotropy respectively. These parameters, expressed as

$$K_p = \frac{2c_{155}}{c_{33}^{(0)}}, \quad K_s = \frac{c_{456}}{c_{44}^{(0)}}, \qquad(19)$$

are controlled by only two nonlinear coefficients c_{155} and $c_{456} = (c_{111} - 3c_{112} + 2c_{123})/8$. Therefore, the shape of the phase velocity surfaces in stressed media is governed by these two coefficients, while the absolute values of velocity (V_{P0}, V_{S0}) are controlled by the third remaining independent coefficient, which may be taken as c_{111}.

"Addition rule."—Equations (16)–(18) show that the Thomsen parameters of stressed rock can be represented as a sum of unstressed (or reference state) anisotropies and stress-induced contributions (denoted by subscript $s–i$). This addition of intrinsic and stress-induced anisotropy in equations (16)–(18) is a manifestation of the general "addition rule," first noticed by Bakulin et al. (2000a) while analyzing the overall anisotropy of VTI rocks with vertical fractures. Comparison of the stress-induced anisotropic coefficients ϵ_{s-i}, δ_{s-i}, and γ_{s-i} in VTI rock with their isotropic counterparts (Rosolofosaon, 1998) reveals their identity, provided $c_{33}^{(0)} - 2c_{44}^{(0)}$ and $c_{44}^{(0)}$ are identified with the Lamé parameters of the isotropic media. Similar to isotropic media (Rasolofosaon, 1998), the stress-

induced components in VTI rocks also satisfy

$$\epsilon_{s-i} = \delta_{s-i},\qquad(20)$$

which is the condition of elliptical anisotropy (Tsvankin, 2001).

We conclude that in the weak anisotropy limit, the following addition rule is applicable to stressed rocks: each anisotropic coefficient of stressed rock is a superposition of the corresponding unstressed (or reference state) coefficient and the stress-induced contribution. The stress-induced part is computed as the anisotropy induced by the current nonhydrostatic stress state in an equivalent isotropic material, resembling the anisotropic rock in its unstressed (or reference) state.

Comparison with experimental data

Jurassic shale.—Hydrostatic stress was used in the shale experiment and the weak-anisotropy approximation predicts a constant amount of anisotropy:

$$\epsilon = \epsilon^{(0)}, \quad \delta = \delta^{(0)}, \quad \gamma = \gamma^{(0)}. \qquad(21)$$

Figure 8 confirms that changes in the anisotropic parameters is less than 0.07 for low confining stress, and less than 0.05 for high confining stress, thus being in qualitative agreement with the weak-anisotropy predictions. However, the background anisotropy of shale is not weak and therefore, exact expressions should be used for quantitative comparison. Theoretically computed anisotropic coefficients, using third-order coefficients from Table 2, show that non-linear elasticity predicts a slight decrease in anisotropic coefficients with increasing level of hydrostatic stress. Figure 8 shows that such a decrease is in good quantitative agreement with the experimental data, and appears to provide a better description of the rock behavior than the weak-anisotropy prediction.

Colton sandstone.—The sample was subjected to biaxial stresses and therefore the magnitude of its anisotropy parameters changed throughout the stress cycle (Figure 9). As predicted by weak-anisotropy equations, the Thomsen parameters start from their unstressed values. For the Colton sample,
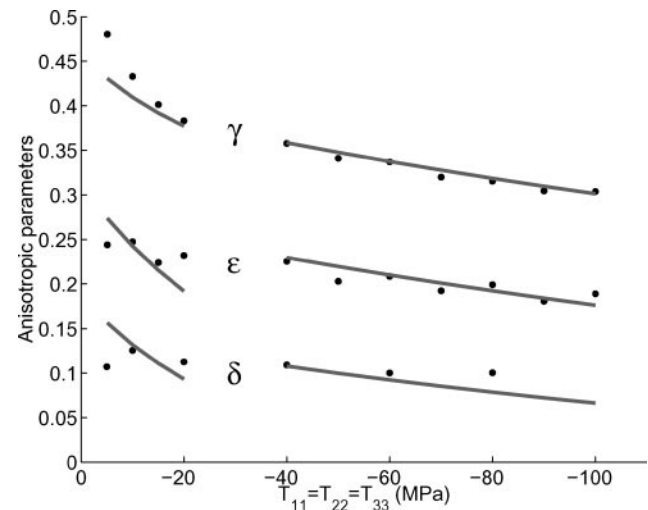

Figure 8. Measured (points) and predicted (lines) Thomsen parameters of Jurassic shale as a function of hydrostatic stress.

both intrinsic and stress-induced anisotropy were small and, therefore, the weak-anisotropy predictions (dotted-dashed lines) are almost indistinguishable from anisotropic parameters computed from exact equations (A-1) (solid lines). Both of them provide a good quantitative description of the experimentally measured anisotropic coefficients, thus confirming the good predictive power of the concise, weak-anisotropy approximations.

When vertical and horizontal loads are unequal, stress-induced contributions ϵ_{s-i}, δ_{s-i}, and γ_{s-i} are negative for $|T_{33}| > |T_{11}|$ and positive for $|T_{33}| < |T_{11}|$ (both T_{11} and T_{33} are assumed compressive). The sign of the stress-induced contribution is controlled by the nonlinear constants c_{155} and c_{456}, which are both typically negative for rocks. In addition, ϵ_{s-i} and δ_{s-i} are equal in the limit of the weak anisotropy, indicating that the stress-induced part of the anisotropy is always elliptical. Comparison of the measured and predicted Thomsen parameters ϵ and γ of biaxially stressed Colton sandstone confirms the predictive power of our model, based on nonlinear elasticity. We find that the coefficients ϵ and γ linearly increase from their unstressed values proportional to $T_{11} - T_{33}$.

CONCLUSIONS

In this study, we presented a concise and comprehensive way of modeling the anisotropic seismic velocities as a function of a 3D stress field, based on nonlinear elasticity theory. The advantages of this modeling scheme are:

1) The behavior of the entire stiffness tensor is modeled as a function of arbitrary triaxial stress; which implies that both P and S (S_1 and S_2) velocities are uniformly treated using the same physical framework. As a result, any velocity in any direction can be predicted as a function of any stress.
2) The model handles an arbitrary triaxial stress state ($T_{11} \neq T_{22} \neq T_{33}$).
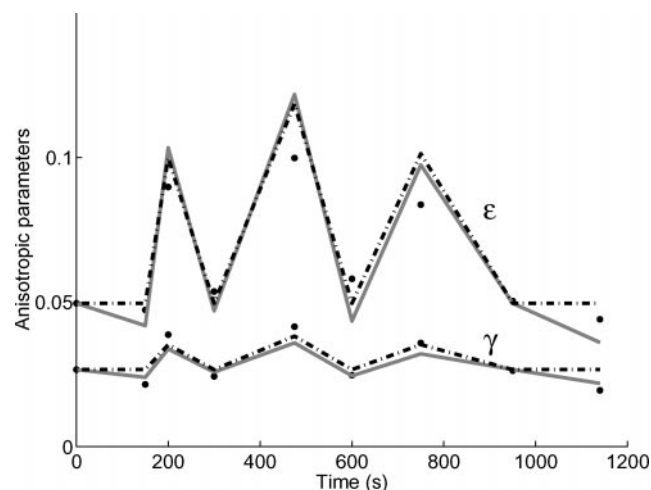3) Intrinsic anisotropy of unstressed formations is taken into account.

Figure 9. Thomsen parameters of Colton sandstone as a function of time throughout the stress cycle from Figure 4. Points are experimental values, dash-dotted lines are prediction by weak-anisotropy approximations (16) and (18); solid lines are prediction by exact equations of nonlinear elasticity.

4) Only three coefficients (nonlinear constants) are required to describe the stress dependence in addition to the five VTI constants.
5) Calibration of the model may be performed using either laboratory techniques on cores or in situ measurements by multimode borehole acoustics (Sinha, 1998, 2002).

The proposed model was applied to explain the stress-dependence of VTI stiffness tensors measured on Jurassic shale (Hornby, 1998) and Colton sandstone (Dillen et al., 1999). The shale was subjected to hydrostatic stress while the sandstone was loaded bi-axially with equal horizontal stresses. As one of the stresses was aligned with the vertical symmetry axis, both samples preserve their VTI symmetry throughout the loading cycle. We demonstrated that nonlinear elasticity correctly explains experimental observations of approximately equal sensitivity of shear-wave velocity to stresses in the polarization and propagation directions.

We developed a weak-anisotropy approximation for Thomsen parameters of stressed rock, predicting that the overall anisotropy is simply a sum of intrinsic and stress-induced parts. For bi-axial stress, changes in each Thomsen coefficient are proportional to the difference between horizontal and vertical stress. For hydrostatic stress ($T_{11} = T_{22} = T_{33}$), the weak-anisotropy approximation predicts that each anisotropic parameter stays equal to its unstressed value. This prediction was qualitatively confirmed for the sample of Jurassic shale, where Thomsen parameters ϵ, δ, and γ were almost insensitive to hydrostatic effective stress. However, the experimentally observed slight decrease in Thomsen parameters versus stress is better described by the exact equations of nonlinear elasticity that account for nonweak, intrinsic anisotropy.

In real rocks, stress dependence comes from a variety of mechanisms: stress dependence of underlying mineral grains, nonwelded grain boundaries, compliant pores and cracks, etc. Nonlinear elasticity is known to mimic the macro behavior of some of these microstructural mechanisms. For example, the behavior of a random pack of spheres under stress and the phenomenon of crack closure in materials with random cracks both closely resemble the nonlinear elasticity type of behavior (Schwartz et al., 1994). We hope that nonlinear elasticity may also absorb the remaining mechanisms, thus providing an "effective medium" description with a small number of nonlinear parameters. The alternative way of describing each of the microstructural mechanisms separately may be overwhelmingly complicated and would probably require a significant number of loosely controlled parameters. If those microstructural parameters are not of primary importance, we believe that nonlinear elasticity approximated through the use of "isotropic" third-order coefficients may serve as a viable theory for the estimation of pore pressure and 3D stress from seismic reflection data (Bakulin et al., 2003).

APPENDIX A

EFFECTIVE ELASTIC CONSTANTS IN REFERENCE CONFIGURATION

Referred to the reference state, the effective elastic constants $c_{ijk\ell}$ given by nonlinear elasticity theory are expressed as (Thurston, 1974; Sinha and Kostek, 1996)

$$c_{1111} = c_{11}^0(1 + 2E_{11}) + T_{11} + c_{111}E_{11} + c_{112}(E_{22} + E_{33}),$$

$$c_{2222} = c_{11}^0(1 + 2E_{22}) + T_{22} + c_{111}E_{22} + c_{112}(E_{11} + E_{33}),$$

$$c_{3333} = c_{33}^0(1 + 2E_{33}) + T_{33} + c_{111}E_{33} + c_{112}(E_{11} + E_{22}),$$

$$c_{1122} = c_{2211} = c_{12}^0(1 + E_{11} + E_{22}) + c_{112}(E_{11} + E_{22})$$
$$+ c_{123}E_{33},$$

$$c_{1133} = c_{3311} = c_{13}^0(1 + E_{11} + E_{33}) + c_{112}(E_{11} + E_{33})$$
$$+ c_{123}E_{22},$$

$$c_{2233} = c_{3322} = c_{13}^0(1 + E_{22} + E_{33}) + c_{112}(E_{22} + E_{33})$$
$$+ c_{123}E_{11},$$

$$c_{1212} = c_{66}^0(1 + 2E_{22}) + T_{11} + c_{144}E_{33} + c_{155}(E_{11} + E_{22}),$$

$$c_{2121} = c_{66}^0(1 + 2E_{11}) + T_{22} + c_{144}E_{33} + c_{155}(E_{11} + E_{22}),$$

$$c_{1221} = c_{2112} = c_{66}^0(1 + E_{11} + E_{22}) + c_{144}E_{33}$$
$$+ c_{155}(E_{11} + E_{22}),$$

$$c_{1313} = c_{44}^0(1 + 2E_{33}) + T_{11} + c_{144}E_{22} + c_{155}(E_{11} + E_{33}),$$

$$c_{3131} = c_{44}^0(1 + 2E_{11}) + T_{33} + c_{144}E_{22} + c_{155}(E_{11} + E_{33}),$$

$$c_{1331} = c_{3113} = c_{44}^0(1 + E_{11} + E_{33}) + c_{144}E_{22}$$
$$+ c_{155}(E_{11} + E_{33}),$$

$$c_{2323} = c_{44}^0(1 + 2E_{33}) + T_{22} + c_{144}E_{11} + c_{155}(E_{22} + E_{33}),$$

$$c_{3232} = c_{44}^0(1 + 2E_{22}) + T_{33} + c_{144}E_{11} + c_{155}(E_{22} + E_{33}),$$

$$c_{2332} = c_{3223} = c_{44}^0(1 + E_{22} + E_{33}) + c_{144}E_{11}$$
$$+ c_{155}(E_{22} + E_{33}). \tag{A-1}$$

T_{ij} and E_{ij} are principal stresses and strains, respectively, which are related by the conventional linear Hooke's law

$$\begin{pmatrix} T_{11} \\ T_{22} \\ T_{33} \\ T_{23} \\ T_{13} \\ T_{12} \end{pmatrix} = \begin{pmatrix} c_{11}^0 & c_{12}^0 & c_{13}^0 & 0 & 0 & 0 \\ c_{12}^0 & c_{11}^0 & c_{13}^0 & 0 & 0 & 0 \\ c_{13}^0 & c_{13}^0 & c_{33}^0 & 0 & 0 & 0 \\ 0 & 0 & 0 & c_{44}^0 & 0 & 0 \\ 0 & 0 & 0 & 0 & c_{44}^0 & 0 \\ 0 & 0 & 0 & 0 & 0 & c_{66}^0 \end{pmatrix} \begin{pmatrix} E_{11} \\ E_{22} \\ E_{33} \\ E_{23} \\ E_{13} \\ E_{12} \end{pmatrix}.$$
$$\tag{A-2}$$

We adopt the convention that compressive stress has a negative sign while tensile stress is positive (Sinha and Kostek, 1996). For large stress levels, it becomes necessary to include second-order (nonlinear) terms in Hooke's law (Thurston, 1974); however in this study, as well as in most other cases, the influence of the higher-order terms on the resulting effective stiffness tensor is small and can safely be neglected.

From equations (A-1), we notice immediately that the effective stiffness tensor for a stressed medium lacks the usual symmetry, since $c_{ijkl} \neq c_{jikl}, c_{ijk\ell} \neq c_{ij\ell k}$ and $c_{ijk\ell} \neq c_{ji\ell k}$. Therefore, strictly speaking, a stressed medium is not exactly equivalent to any intrinsically anisotropic solid. The asymmetry is caused by the presence of the terms $c_{ij}^{(0)}E_{kl}$ and T_{mn}; these terms are typically much smaller than the remaining terms of form $c_{ij}^{(0)}$ and $c_{ijk}E_{mn}$ because, for rocks, $c_{ijk} \gg c_{mn}^{(0)} \gg T_{pq}$. The degree of this asymmetry (ratio of "asymmetric" terms to overall value of effective elastic constant) is typically less than 0.1% in stiffness or 0.05% in velocity (Thurston, 1974; Rasolofosaon, 1998). Such asymmetry is below the accuracy of the seismic method and may safely be ignored, so that equations (A-1) reduce to a description of an orthorhombic solid approximated by equations (1).

Another representation can be found in the literature which refers second- and third-order tensors to the intermediate configuration (Sinha, 1982; Rasolofosaon, 1998). For small deformations and small deformation gradients, equations in the intermediate configuration differ from equations (A-1) only by small terms ($c_{ij}^{(0)}E_{k\ell}$ and T_{ij}). As before, neglecting these terms leads to the same approximated equations (1).

APPENDIX B

HYDROSTATIC STRESS EXPERIMENT

Isotropic rocks

Many laboratory experiments on rocks are performed under hydrostatic stress ($T_{11} = T_{22} = T_{33}$). In intrinsically isotropic media, a hydrostatic stress field produces a hydrostatic strain $E_{11} = E_{22} = E_{33}$. Substituting intrinsic isotropy conditions for our background VTI media ($c_{11}^0 = c_{33}^0, c_{44}^0 = c_{66}^0, c_{13}^0 = c_{12}^0$) in equations (1), we find similar isotropic conditions for stressed media $c_{11} = c_{22} = c_{33}, c_{12} = c_{13} = c_{23}, c_{44} = c_{55} = c_{66}$, and $c_{11} = c_{44} + 2c_{12}$; that is, as intuitively expected, isotropic rock under hydrostatic stress remains isotropic. Therefore, at each level of stress, hydrostatic experiments on isotropic rocks can provide us with only two independent parameters c_{11} and c_{44}, and we cannot recover the three unknown third-order coefficients. We conclude that hydrostatic stress experiments for intrinsically isotropic rocks are not capable of providing all three nonlinear parameters needed to describe the anisotropic stiffness tensor at arbitrary stress, without invoking some microscopic crack closure (Mavko et al., 1995) or a grain contact model (Schwartz et al., 1994) for rock stiffening.

Hydrostatic stress experiments in VTI rocks

As previous studies focused on the analysis of velocities propagating in a single direction, they used a "best-fit" isotropic approximation of Hooke's law (A-2) for converting strains to stresses in intrinsically anisotropic materials (Guz et al., 1977) and rocks (Bakulin and Protosenya, 1982; Bakulin et al.,

2000b). They also assumed isotropic form of the third-order tensor which requires only three nonlinear constants. Nevertheless, with the isotropic approximation for Hooke's law it is still impossible to recover all three nonlinear coefficients from the hydrostatic stress experiment.

We also use the latter assumption of isotropic third-order tensor that has been proven to be sufficient for explaining stress-dependent velocities in most anisotropic materials (Johnson and Rasolofosaon, 1996; Sinha and Kostek, 1996; Winkler and Liu, 1996; Bakulin et al., 2000b; Sarkar et al., 2003). However, in contrast to references above, we focus on the behavior of the P- and S-wave velocities in all directions and thus use the exact VTI Hooke's law (A-2), which helps to avoid the above-mentioned nonuniqueness associated with the estimation of the third-order coefficients using hydrostatic stress states. For VTI media, the hydrostatic stress field ($T_{11} = T_{22} = T_{33}$) results in a nonhydrostatic strain field because $E_{11} = E_{22} \neq E_{33}$. Visual inspection of the equations (1) shows that, in contrast with the isotropic case, five linearly independent equations with three unknowns are available for inversion. Note that, although theoretically any amount of intrinsic anisotropy removes the ambiguity, in practice the anisotropy should be sufficient to produce a well-conditioned set of equations in the presence of experimental errors. We experimentally quantify this "sufficient" amount of intrinsic anisotropy in the section "Colton sandstone."

We conclude that assuming VTI anisotropy of an unstressed rock actually helps us to avoid the ambiguity existing for isotropic media, allowing us to constrain all three nonlinear coefficients even from a hydrostatic stress experiment.

REFERENCES

Bakulin, A., and Bakulin, V., 1992, Method for determining rock mass burst danger: USSR Patent 1 786 273.

Bakulin, V., and Bakulin, A., 1999, Acoustopolarizational method of measuring stress in rock mass and determination of Murnaghan constants: 69th Annual International Meeting, SEG, Expanded Abstracts, 1971–1974.

Bakulin, V., and Protosenya, A., 1981, Ultrasonic polarizational method of determination of stress in rock mass: Mining Geophysics (in Russian), 96–97.

——— 1982, Nonlinear effects in travel of elastic waves through rocks: Proceedings of the USSR Academy of Sciences, (Doklady Akademii Nauk SSSR), **263 (2)**, 214–316.

Bakulin, A., Grechka, V., and Tsvankin, I., 2000a, Estimation of fracture parameters from reflection seismic data—part II: Fractured models with orthorhombic symmetry: Geophysics, **65**, 1803–1817.

Bakulin, A., Troyan, V., and Bakulin, V., 2000b, Acoustoelasticity of rocks: St. Petersburg University Press (in Russian).

Bakulin, A., Sinha, B., and Prioul, R., 2003, System and method for estimating subsurface principal stresses from seismic reflection data:

US Patent application publication US 2003/0125878 A1.

Bowers, G., 1995, Pore pressure estimation from velocity data: Accounting for overpressure mechanisms besides undercompaction: SPE Drilling and Completion, **10**, 89–95.

Dillen, M. W. P., Cruts, H. M. A., Groenenboom, J., Fokkema, J. T., and Duijndam, A. J. W., 1999, Ultrasonic velocity and shear-wave splitting behavior of a Colton sandstone under a changing triaxial stress: Geophysics, **64**, 1603–1607.

Dutta, N. C., 2002, Geopressure prediction using seismic data: Current status and the road ahead: Geophysics, **67**, 2012–2041.

Eaton, B. A., 1975, The equation for geopressure prediction from well logs: SPE Paper 5544, 1–11.

Eberhart-Phillips, D., Han, D., and Zoback, M. D., 1989, Empirical relationships among seismic velocity, effective pressure, porosity, and clay content in sandstone: Geophysics, **54**, 82–89.

Guz, A. N., Makhort, F. G., and Guscha, O. I., 1977, Introduction to acoustoelasticity: Kiev "Naukova dumka" (in Russian).

Hornby, B. E., 1995, The elastic properties of shales: Ph.D. dissertation, Cambridge University.

Hornby, B. E., 1998, Experimental laboratory determination of the dynamic elastic properties of wet, drained shales: Journal of Geophysical Research, **103**, 945–964.

Johnson, P. A., and Rasolofosaon, P. N. J., 1996, Nonlinear elasticity and stress-induced anisotropy in rocks: Journal of Geophysical Research, **101**, 3113–3124.

Mavko, G., Mukerji, T., and Godfrey, N., 1995, Predicting stress-induced velocity anisotropy in rocks: Geophysics, **60**, 1081–1087.

Press, W., Flannery, B., Teukolsky, S., and Vetterling, W., 1986, Numerical recipes: The art of scientific computing: Cambridge University Press.

Rasolofosaon, P., 1998, Stress-induced seismic anisotropy revisited: Revue de l'Institut Français du Pétrole, **53**, 679–692.

Sarkar, D., Bakulin, A., and Kranz, R., 2003, Anisotropic inversion of seismic data for stressed media: Theory and a physical modeling study on Berea Sandstone: Geophysics, **68**, 690–704.

Schwartz, L. M., Murphy, W. F. I., and Berryman, J. G., 1994, Stress-induced transverse isotropy in rocks: 64th Annual International Meeting, SEG, Expanded Abstracts, 1081–1085.

Sinha, B. K., 1982, Elastic waves in crystals under a bias: Ferroelectrics, **41**, 61–73.

——— 1998, Method for estimating formation in-situ stress magnitude using a sonic borehole tool: US Patent 5 838 633.

Sinha, B. K., Kane, M. R., and Frignet, B., 2000, Dipole dispersion crossover and sonic logs in a limestone reservoir: Geophysics, **65**, 390–407.

Sinha, B. K., and Kostek, S., 1996, Stress-induced azimuthal anisotropy in borehole flexural waves: Geophysics, **61**, 1899–1907.

——— 2002, Determining stress parameters of formations from multi-mode velocity data: US Patent 6 351 991.

Thomsen, L., 1986, Weak elastic anisotropy: Geophysics, **51**, 1954–1966.

Thurston, R., 1974, Waves in solids *in* Truesdell, W., Ed., Encyclopedia of physics: Springer-Verlag, VIa4.

Tsvankin, I., 2001, Seismic signatures and analysis of reflection data in anisotropic media: Elsevier Science Publishing Co.

Wang, Z., 2002, Seismic anisotropy in sedimentary rocks, part 2: Laboratory data: Geophysics, **67**, 1423–1440.

Winkler, K., and Liu, X., 1996, Measurements of third-order elastic constants in rocks: Journal of the Acoustic Society of America, **100**, 1392–1398.

Winkler, K. W., Sinha, B. K., and Plona, T. J., 1998, Effects of borehole stress concentrations on dipole anisotropy measurements: Geophysics, **63**, 11–17.